Effect of silica leaching treatment during template-assisted synthesis on the performance of FeNC catalysts for oxygen reduction reaction

Electrochimica Acta 525 (2025) 146085

Contents lists available at ScienceDirect

Electrochimica Acta

journal homepage: www.journals.elsevier.com/electrochimica-acta

Effect of silica leaching treatment during template-assisted synthesis on the performance of FeNC catalysts for oxygen reduction reaction

Giulia Gianola [a,b,*], Alessio Cosenza [c], Camille Roiron [c], Candido F. Pirri [a,b], Stefania Specchia [b], Plamen Atanassov [c], Juqin Zeng [a,b,*]

[a] Center for Sustainable Future Technologies, Istituto Italiano di Tecnologia, Via Livorno, 60, 10144, Torino, Italy
[b] Department of Applied Science and Technology (DISAT), Politecnico di Torino, Corso Duca degli Abruzzi, 24, 10129, Torino, Italy
[c] Department of Chemical and Biomolecular Engineering, University of California, Irvine, 92697, CA, United States

ARTICLE INFO

Keywords:
Iron-nitrogen-carbon catalyst
Oxygen reduction reaction
Silica removal
Mesoporous
Activity

ABSTRACT

The development of cost-effective and environmentally sustainable electrocatalysts is crucial for advancing the commercialization of proton exchange membrane fuel cells (PEMFCs). In this work, we investigate the effect of different silica leaching strategies on the synthesis of iron-nitrogen-carbon (FeNC) electrocatalysts for the oxygen reduction reaction (ORR). Three FeNC samples were prepared using SBA-15 mesoporous silica as the template and subjected to varying removal techniques: hydrofluoric acid (HF), sodium hydroxide followed by hydrochloric acid (NaOH+HCl), and an acid-free Teflon-assisted process. Physical-chemical characterization reveals significant differences in the surface area and porosity of the three catalysts. The specific surface areas of FeNC treated with NaOH+HCl and HF are 1352 m^2/g and 1403 m^2/g, respectively, while the Teflon-treated sample exhibits a much lower value of 732 m^2/g. Electrochemical tests using a rotating ring disk electrode (RRDE) apparatus demonstrate superior ORR activity of the FeNC treated with NaOH+HCl, achieving onset potentials of 0.93 V_{RHE} and 0.81 V_{RHE} in alkaline and acidic media, respectively, outperforming the HF- and Teflon-treated counterparts. The HF treatment, while effective in removing silica and metallic impurities, poses environmental and safety challenges. The Teflon-assisted approach, despite its promise as a greener alternative, results in a lower surface area and diminished ORR activity, with onset potentials of 0.89 V_{RHE} and 0.76 V_{RHE} in alkaline and acidic media, respectively. This study highlights the importance of optimizing silica removal methods to balance the catalyst performance, safety and sustainability, with the NaOH+HCl method emerging as the most effective approach for producing high-performance FeNC ORR catalysts for fuel cell applications.

1. Introduction

In the need for sustainable energy conversion devices, fuel cells (FCs) have attracted more and more interest in recent years because of their high efficiency and low environmental impact [1,2]. Among all types of FCs, proton exchange membrane FCs (PEMFCs) have gained significant importance due to their versatility, high power density, and suitability for a wide range of applications. However, the commercialization of PEMFCs is still hindered by the high cost of the materials required for their fabrication [3,4]. One of the main limitations comes from the cathode side, where oxygen reduction reaction (ORR) takes place. The sluggish kinetics of ORR requires high loadings of platinum (Pt)-based electrocatalysts to achieve sufficient performance. No other materials have been found to be as effective as Pt for ORR electrocatalysis [5]. However, its prohibitively high cost and limited availability present a big barrier to the large-scale commercialization of PEMFCs. The need for alternative electrocatalysts has pushed scientific research toward Metal-Nitrogen-Carbon (MNC) materials as cost-effective and green solutions for ORR [6–8].

Among the reported MNC electrocatalysts, single-atom FeNC has become particularly promising for its high activity [9]. The coordination of iron atoms with nitrogen moieties within a carbon matrix offers several advantages in terms of electrocatalytic activity and stability [10,11]. Even if the nature of active sites for ORR is still under debate, many researchers address the activity of FeNC electrocatalysts on Fe-moieties and Fe-free moieties [12–14]. The most recognized contribution comes from single Fe atoms coordinated by a variable number of N atoms, constituting Fe-N_x active sites located in vacancies inside the carbon

* Corresponding authors.
E-mail addresses: giulia.gianola@iit.it (G. Gianola), juqin.zeng@polito.it (J. Zeng).

https://doi.org/10.1016/j.electacta.2025.146085
Received 19 November 2024; Received in revised form 28 February 2025; Accepted 19 March 2025
Available online 21 March 2025

matrix. Indeed, nitrogen is very important for the electrocatalytic properties of FeNC electrocatalysts [15], such that identifying the role of N species allows the customization of the properties of the electrocatalyst itself. In addition to Fe-N_x active sites, other Fe-moieties may also have a role towards ORR, like Fe-carbides or Fe-containing nanoparticles [11]. Moreover, metal-free sites (N-pyridinic, N-graphitic, N-pyrrolic) have been debated as a further active center for ORR [11].

According to the literature, the most common approach for FeNC synthesis involves the pyrolysis of iron-, nitrogen-, and carbon-containing precursors after previous mixing in a solvent. The materials decompose and react to form FeNC active sites thanks to the high-temperature treatment in an inert atmosphere, usually ranging from 600 to 1000°C [11,16,17]. To control the morphology of the catalyst, a template assisted synthesis approach is commonly used. Templates such as silica, zeolites, or block copolymers are used to shape the precursor materials. Iron-, nitrogen-, and carbon-containing precursors are incorporated into the template, which is then subjected to pyrolysis. Following this high-temperature treatment, the template is removed, usually by chemical etching or calcination, resulting in an electrocatalyst with a porous structure tailored by the template [18–20].

In this work, we propose a synthesis strategy based on the utilization of mesoporous silica as the template for tailoring the morphology and porosity of the electrocatalyst. Silica can be easily tailored to have specific pore sizes, shapes, and structures and it is also thermally stable at high temperatures, essential during the pyrolysis step. Other templates like organic polymers do not offer the same advantages: they might provide some tunability, but their pore structures are generally less defined and harder to control, also due to the poor thermal stability that can lead to the decomposition of the template and the collapse of the pore structure [21]. Furthermore, silica also offers the advantage of being chemically inert during the synthesis process, preserving the purity of the final electrocatalyst. Other templates, like metal-organic frameworks, can interact with the electrocatalyst precursors, introducing impurities or altering the chemical composition of the final electrocatalyst [22,23]. One of the major issues related to this kind of template is the complete removal of the silica after the heat treatment. Here three different approaches to remove the silica template are investigated. The first two rely on the effects of acid and basic washing methods for silica removal, widely discussed in the literature [13–15]. Concerning acid treatment, hydrofluoric acid (HF) reacts with silicon dioxide (SiO_2) to form silicon tetrafluoride (SiF_4) gas and water, according to the following reaction [24]:

$$SiO_2+4HF\rightarrow SiF_4\uparrow+2H_2O \quad (1)$$

Usually, the electrocatalyst-silica powder is immersed in an HF aqueous solution (5 % to 10 %). In this way, the silica is etched out through the formation of SiF_4 gas while preserving the structure of the template. This process is highly efficient for complete silica removal, but HF is an extremely toxic compound and can cause severe health issues. It is also highly corrosive to most materials and environmentally hazardous [25]. To overcome this safety issue, in this work, we compare the effect of HF leaching with another washing technique based on the utilization of sodium hydroxide (NaOH), a safer and more environmentally friendly solution for silica removal [15]. NaOH effectively dissolves silica by converting it into water-soluble silicate species, according to the following reaction:

$$SiO_2+2NaOH\rightarrow Na_2SiO_3(\text{soluble silicate})+H_2O \quad (2)$$

Lastly, we also use an acid-washing-free synthesis, where Teflon (PTFE) is mixed with the precursors and used to remove the sacrificial template. This technique, developed by Atanassov's group at the University of California Irvine [26], leads to a more sustainable and intensified synthesis strategy compared to the traditional method, allowing the removal of the silica template thanks to the *in-situ* Teflon decomposition at high temperatures. When Teflon is incorporated in the precursors' mix and subjected to pyrolysis, it decomposes at temperatures higher than 500°C, releasing various fluorocarbon gasses, such as tetrafluoroethylene (C_2F_4), hexafluoropropylene (C_3F_6) and HF that can react with silica. The reaction of HF with silica leads to the formation of volatile silicon tetrafluoride (SiF_4) and other fluorosilicates, according to reaction (1), promoting the total removal of the silica template. The volatile by-products are *in-situ* removed by the nitrogen flushing during the heat treatment, leaving behind the porous FeNC electrocatalyst structure [27,28].

Another challenge in the synthesis of FeNC electrocatalysts is the formation of iron nanoparticles during heat treatment at high temperatures. While these nanoparticles may not directly impact the electrocatalytic performance, they can undergo oxidation or corrosion during electrocatalytic cycling, leading to their leaching from the electrocatalyst layer. This process promotes undesired side reactions [29,30], therefore, minimizing or removing metal particles through optimized synthesis techniques and post-treatment methods is crucial for enhancing FeNC electrocatalysts in ORR applications. In this context, acid leaching plays again an important role. HF can be effective not only for silica template removal, as explained before, but it can also dissolve and remove metal particles from the surface or the bulk of the electrocatalyst. In particular, the acid reacts with the metal particles leading to soluble metal salts or complexes, finally removed through washings with deionized water [31]. In the case of the NaOH-treated sample, the basic washing alone is insufficient for the metal particle removal. As a valid alternative to toxic HF, we combine the NaOH leaching with a hydrochloric acid (HCl)-based washing step [15,32]. HCl effectively reacts with metallic iron and iron oxides to form soluble iron chloride salts according to the following reactions:

$$Fe + 2HCl \rightarrow FeCl_2+ H_2\uparrow \quad (3)$$

$$Fe_2O_3+6HCl\rightarrow 2FeCl_3+3H_2O \quad (4)$$

$$Fe_3O_4+8HCl\rightarrow FeCl_2+2FeCl_3+4H_2O \quad (5)$$

These soluble iron chlorides are then easily washed away during subsequent rinsing steps, effectively purifying the electrocatalyst. The controlled removal of iron nanoparticles through HCl etching restores and enhances the porosity of the carbon matrix, ensuring greater accessibility of reactants to the active sites. Similarly, a leaching step would typically be required for the Teflon-treated sample to remove residual iron nanoparticles. However, as demonstrated by Cosenza et al. [26], additional acid leaching after the heat treatment does not result in any significant improvement in the electrochemical performance. Therefore, this step was omitted in the present work.

Among all the silica templates, SBA-15 has been chosen for this work. In comparison to other silica templates, like MCM-41, SBA-15 presents larger and more uniform pores [23]. Large pores imply a better mass transport of reactants and products, enhancing the accessibility of the active sites. Because of the high specific surface area of SBA-15, more active sites are provided for electrocatalysis [22]. Moreover, SBA-15 has thicker pore walls, making it more stable from a thermal point of view. Here, we present three FeNC electrocatalysts achieved with different synthesis strategies, starting from the same SBA-15 template: $FeNC^{HF}$, $FeNC^{NaOH+HCl}$, and $FeNC^{Teflon}$. The materials are characterized by several physical-chemical methods to investigate their composition, morphology, and porous structure, while the electrochemical characterization has been performed with rotating disk electrode (RDE) and rotating ring disk electrode (RRDE) setups in both alkaline and acidic environments. Among all the synthesis strategies presented here, $FeNC^{NaOH+HCl}$ results as the most performant electrocatalyst in both acid and alkaline media.

2. Materials and methods

2.1. Synthesis of the SBA-15 silica template

Hexagonal mesoporous SBA-15 was synthesized following the method reported by Zhao et al. [33]. To this purpose, 4 g of poly (ethylene glycol)-*block*-poly(propylene glycol)-*block*-poly(ethylene glycol) (Pluronic P123, average M_n~5800, Sigma Aldrich) were dispersed in a solution of 136 ml of ultrapure water (18.2 MΩ resistivity) and 19.42 ml of hydrochloric acid (HCl, 37 wt %, Sigma Aldrich) at 40°C for 6 hours. Then, 9.6 ml of tetraethylorthosilicate (TEOS, 98 wt %, Sigma Aldrich) was added to the reactor and stirred at 40°C for 20 hours. The mixture was then placed in an oven at 100°C for 24 hours where a hydrothermal process occurred. The sample was then filtered and washed with water in a vacuum filtration setup. After drying, the product was calcined in air in a static oven for 10 hours at 550°C to remove the surfactants.

2.2. Synthesis of the FeNC electrocatalysts

For each sample, 500 mg of synthesized SBA-15 were dispersed at room temperature in 20 ml of ultrapure water and ethanol (v:v=1:1) in one beaker. In another beaker, 400 mg of iron (III) nitrate nonahydrate ($Fe(NO_3)_3{\cdot}9H_2O$, purity > 98 %, Sigma Aldrich) were dissolved in 10 ml of water and ethanol (v:v=1:1) to get a yellowish solution, followed by the addition of 492 mg of 1,10 phenanthroline (anhydrous for synthesis, Sigma Aldrich) to form a red solution. Then, the SBA-15 suspension was added to the precursors' solution. The mixture was left under stirring at 75°C for 24 hours to evaporate the solvents. Subsequently, the synthesis proceeds differently for each sample:

- $FeNC^{HF}$: The collected powder was placed in a tubular oven under a N_2 atmosphere and heated up to 900°C with a heating ramp of 5°C min^{-1} and a dwell time of 3 hours to decompose the Fe-phen complex and form FeNC structure in the hexagonal SBA-15 template. The powder was leached in a solution of 35 ml of hydrofluoric acid (HF, 40 wt %, Sigma Aldrich) and 20 ml of water for 48 hours to remove the silica template and etch iron or oxide nanoparticles. Then, 15 ml of HF (40 wt %) were added to the previous solution, leaving the etching process for another 48 hours. The suspension was centrifuged and washed with water till a pH > 4 was achieved. Finally, the electrocatalyst was dried overnight at 80°C and then collected.
- $FeNC^{NaOH+HCl}$: The sample was placed in a tubular oven to be subjected to the same pyrolysis step described for the $FeNC^{HF}$ sample. Then, the powder was dispersed at room temperature in a 2 M sodium hydroxide (NaOH, Macron Fine Chemicals, 95.0–100 % pellets) solution of 160 ml of water and ethanol (v:v=1:1) for 24 hours to remove the silica template. The material was then washed with water in a centrifuge to remove NaOH. The collected sample was stirred in 100 ml of hydrochloric acid (HCl, 37 %, Sigma Aldrich) at room temperature for 3 hours to remove metal or oxide nanoparticles. Finally, the material was collected and washed with water and ethanol by centrifugation and dried overnight at 80°C.
- $FeNC^{Teflon}$: Polytetrafluoroethylene powder (Teflon, 1 μm particle size, Sigma Aldrich) was added to the collected powder. The amount of Teflon was computed relatively to the wt % of silica according to Cosenza et al. [26]. The mixture was ball milled for 1 hour at 10 Hz and then collected.

Finally, all three collected powders were subjected to a pyrolysis step run again under an N_2 atmosphere and heated up to 900°C with a heating ramp of 5°C min^{-1} and a dwell time of 3 hours to improve the graphitization degree of the electrocatalysts.

2.3. Physical-chemical characterization

Powder X-ray diffraction (XRD) was achieved through a Rigaku powder X-ray diffractometer with a Cu Kα radiation (0.15418 nm) at 40 kV voltage, 30 mA current, and a nickel K-beta filter. The step size was 0.03° and 2θ varied from 20° to 90° The identification of the phases was based on the PDXL software and ICDD database. Transmission Electron Microscopy (TEM) images were acquired through a JEOL JEM-2800 microscope at an accelerating voltage of 200 kV. Scanning Electron Microscopy (SEM) was performed through a FEI Magellan 400 XHR SEM to obtain images of the surface morphology of the synthesized materials. The selected current ranged from 50 pA to 0.80 nA, the voltage varied between 10 kV and 20 kV, and both the ETD (Everhart-Thornley detector) and TLD (through-the-lens detector) detectors were used. The materials' surface chemistry and composition were analyzed using X-ray Photoelectron Spectroscopy (XPS) with a Kratos AXIS Supra instrument. An Al Kα beam (1486.6 eV) was employed at 15 mA and 225 W. Scans, recorded with a spot of 300 × 700 μm size, were conducted from 0 to 1400 eV for survey scans, 270 to 300 eV for C 1 s detailed scans, 390 to 415 eV for N 1 s detailed scans, 702 to 740 eV for Fe 2p detailed scans, and 525 to 543 eV for O 1 s detailed scans. All the collected spectra were obtained under identical conditions, with the samples placed in an ultrahigh vacuum chamber at 5 10^{-8} mmHg, and calibrated against a value of the C 1 s binding energy of 284.5 eV. Elemental analysis of the surface was performed using CasaXPS software. A linear background was applied to the C 1 s, N 1 s, and O 1 s regions, while a Shirley background was used for the Fe 2p 3/2 region. Peak analysis employed a Gaussian/Lorentzian function (70 %/30 %). Iron contents in the final materials were obtained by Inductively Coupled Plasma Mass Spectroscopy (ICP-MS) of digested electrocatalysts. A known amount of each powder (between 2 and 3 mg) was placed in a Teflon reactor with 10 mL of Aqua Regia freshly prepared (1:3 HNO_3:HCl, HNO_3 67–70 % vol. and HCl 34–37 % vol. both TraceMetal grade, Fisher Chemical). The reactors were closed tight and placed in a Mars 7 CEM microwave. The temperature was raised to 250°C in 30 min. After a 1 h hold and natural cool down, the digested samples were placed in a vial with 40 mL of water used to rinse the reactor. The Fe concentration of this solution was measured using ICP-MS after a 5 % vol. dilution in 1 % vol. HNO_3. The ICP-MS measurements were done in STD mode on a Thermo Scientific ICP-MS. Raman spectroscopy was performed using an InVia Raman spectrometer (Renishaw) equipped with a 785 nm near-infrared laser. A 50x objective lens was used to focus the laser beam onto the sample surface. Spectra were acquired with a 30 s exposure time over a wavenumber range of 1070–2000 cm^{-1}, relevant for characterizing carbon-based catalysts. Post-acquisition data processing was carried out in OriginLab, including baseline correction and peak fitting using Voigt functions. N_2 physisorption curves were acquired on a Micromeritics 3Flex Analyzer at 77 K. 20 to 40 mg of sample were placed in a glassy burette filled with a glassy rod. The samples were degassed for 12 hours at 200°C to remove any species adsorbed on the materials. Then the tube was cooled to liquid nitrogen temperature (77 K) and the analysis was performed. The Barrett-Joyner-Halenda (BJH) method was used to estimate the cumulative pore volume of the electrocatalysts, while the Brunauer-Emmett-Teller (BET) method allowed the calculation of the specific surface area.

2.4. Electrochemical characterization in RRDE

The electrochemical characterizations were recorded at room temperature with a Biologic VSP-300 potentiostat and Pine Research MSR Rotator as the RRDE apparatus. The electrocatalysts were dispersed by ultrasonic mixing in isopropanol (IPA) and a 5 wt % suspension of Nafion® (Ion Power, Inc.), to have an ionomer-to-carbon ratio I/C=0.2. The electrocatalyst-based inks were drop-casted onto a glassy carbon disk/Pt ring working electrode (active area 0.247 cm^2) with a loading of 0.4 mg cm^{-2}. A carbon rod was used as the counter electrode and a

Hydroflex reversible hydrogen electrode (RHE, provided by Gaskatel) was used as the reference electrode. All the measurements were performed in alkaline (0.1 M KOH) and acid (0.1 M $HClO_4$) environments saturated in nitrogen or oxygen according to the specified test. All the potentials are referred to the RHE. Cyclic voltammetry (CV) curves were acquired by cycling the potential between 0 V_{RHE} and 1.1 V_{RHE} at a scan rate of 100 mV s^{-1} in O_2- and N_2-saturated electrolytic solution. 3-electrode configuration (disk/reference/counter) tests were carried out in O_2-saturated electrolyte with linear sweep voltammetry (LSV) curves in the potential range 0–1.1 V_{RHE} at a scan rate of 10 mV s^{-1} with a disk-electrode rotation of 400, 900, 1600, and 2500 rpm. 4-electrode configuration (disk/ring/reference/counter) tests were recorded at 1600 rpm in O_2-saturated electrolyte with LSV by scanning the disk from 0 V_{RHE} to 1.1 V_{RHE} at a scan rate of 10 mV s^{-1} and fixing the ring potential at 1 V_{RHE}. Finally, all the measurements were iR-drop corrected thanks to the value of the series resistance R_s achieved through electrochemical impedance spectroscopy (EIS) measurements. EIS measurements were performed at fixed 1 V_{RHE} potential, with an AC signal of 10 mV amplitude and 10^0–10^6 Hz frequency range. The LSV curves were background-corrected subtracting the LSV recorded in N_2-saturated electrolyte at 10 mV s^{-1} to get rid of capacitive contributions to the reducing current. Koutecky-Levich (KL, see SI) theory has been applied to the $FeNC^{NaOH+HCl}$ to appreciate the effect of the rotation rate and estimate the number of electrons involved in the ORR. Chronoamperometry (CA) tests have been conducted at a fixed potential of 0.68 V_{RHE} and a rotation speed of 1600 rpm to assess catalysts' stability over time. Platinum on graphitized carbon (Pt/C, 20 wt %, Sigma-Aldrich) is used as a benchmark. The ink formulation includes 2.5 mg of Pt/C powder, 1619.4 μL of deionized water (DIW), 1619.4 μL of isopropanol (IPA), and 135.0 μL of 5 wt % Nafion perfluorinated resin solution. 20 μl of ink were deposited onto the glassy carbon disk to have an electrocatalyst loading of 12 μg_{Pt} cm^{-2}.

3. Results and discussion

3.1. Structure and morphology

XRD spectra, shown in Fig. 1, were collected to elucidate the crystalline structure of the synthesized materials. All the electrocatalysts show a sharp graphitic peak at about 26° as a result of the high-temperature graphitization process. The $FeNC^{NaOH+HCl}$ and $FeNC^{HF}$ samples show only one additional peak around 44° ascribed to graphitic carbon, leading to the conclusion that the silica etching steps through liquid solutions were effective for removing metal nanoparticles. In the same way, no reflection around 22°associated with silica is present. However, in the case of $FeNC^{Teflon,}$ several other peaks can be observed and assigned to iron nitride, iron carbide, and iron oxide species [34]. Peaks at 44.6°, 65.1°, and 82.3° are associated respectively with (110), (200), and (211) Fe phases (PDF 1–1267). Peaks at 43.6°, 50.8°, and 74.8° are associated with Fe-C alloys (PDF 23–298), specifically with (111), (200), and (220) facets. The *in-situ* gas phase silica etching during pyrolysis through Teflon decomposition is ineffective for removing metal nanoparticles.

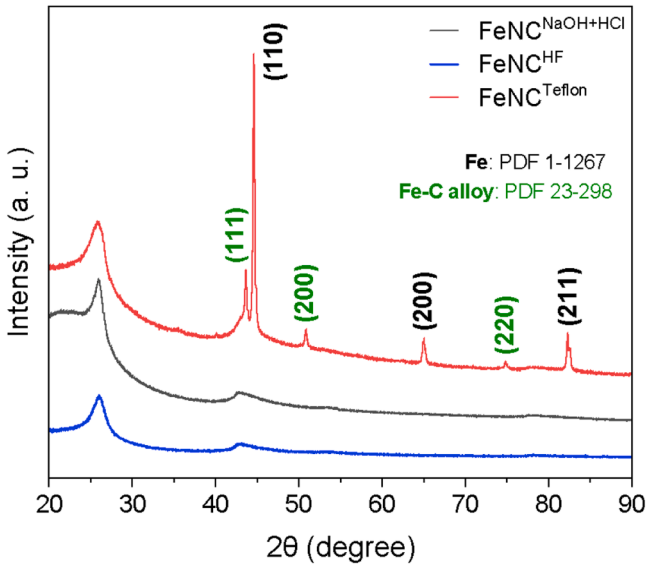

Fig. 1. XRD spectra of the FeNC electrocatalysts.

TEM images were taken for all electrocatalysts (Fig. 2), showing both graphitic and amorphous domains. The presence of iron nanoparticles with size in the range of 40–80 nm was observed only in the case of $FeNC^{Teflon}$, confirming the results of XRD analysis.

The morphology of the porous network of the FeNCs was highlighted through SEM images, in Fig. S1. It is evident from Fig. S1a that the SBA-15 is constituted of smooth 1 μm long subunits interconnected with each other and forming fiber-like structures with length in the range of 10–20 μm and diameter of about 5 μm. The same morphology was observed for $FeNC^{NaOH+HCl}$ and $FeNC^{HF}$, as evident from Fig. S1b and Fig. S1c, respectively, indicating the success of the templating approach for the catalyst synthesis. In the case of $FeNC^{Teflon}$, the three-dimensional structure (Fig. S1d) does not match that of SBA-15. This discrepancy can be ascribed to the fact that the decomposition of Teflon and the subsequent removal of silica occur rapidly at a much lower temperature than that required for the graphitization of the precursors. Consequently, the formation of the graphitic structure happens after the removal of SBA-15, which means that the original template's structure cannot be exactly replicated.

Raman spectroscopy was carried out on FeNC-based samples to evaluate the degree of organization of the carbon. The spectra are reported in Fig. 3a. Each spectrum presents the typical D (~1310 cm^{-1}) and G (~1600 cm^{-1}) bands, highlighting the presence of defects within the sp^2 carbon network and the graphitic (sp^2-bonded carbon) structure, respectively. The fitted spectra (Fig. S2) were used to evaluate the I_D/I_G ratio and the average graphitic cluster diameter (L_α) (Fig. 3b) following the method established by Tuinstra and Koenig [35].

As highlighted in Fig. 3b, $FeNC^{NaOH+HCl}$ and $FeNC^{HF}$ samples show similar I_D/I_G ratios, 1.1 and 1.2 respectively, indicating a higher degree of graphitization to the $FeNC^{Teflon}$ electrocatalyst (I_D/I_G = 2.3). The lower structural order of the Teflon-treated material can be again attributed to the early removal of the silica template, hindering the development of a well-organized graphitic framework. The varying degree of disorder introduced by each treatment is further reflected in the differences in the crystallite size. With comparable L_α values, $FeNC^{NaOH+HCl}$ (~80 Å) and $FeNC^{HF}$ (~76 Å) show the highest graphitization and structural order within the carbon matrix.

The electrocatalysts' surface atomic composition and chemical environment were analyzed through XPS. The sample denoted as $FeNC^{NaOH+HCl}$ shows a relatively high oxygen content and a low carbon content, in favor of a non-negligible amount of silicon (at. % > 4 %) which is reasonably ascribed to the incomplete silica removal coming from the mild silica etching steps based on HCl and NaOH washings. Instead, the HF washing and the Teflon-assisted method allowed a complete template removal and this can be ascribed to the reaction of HF with silica [24,27,28], more effective than the one with NaOH. A successful nitrogen doping can be observed for all the electrocatalysts, ranging from 1.1 at. % to 1.8 at. %. The results are summarized in Table 1.

The examination of the N 1 s and C 1 s spectra was based on methodologies drawn from earlier studies [26,36–39]. The detailed N 1 s spectra were deconvoluted as shown in Fig. S3. They revealed several nitrogen moieties: N pyridinic at 398.5 eV, Fe-nitrogen coordination at 399.4 eV, N pyrrolic at 400.8 eV, N graphitic at 401.8 eV, N quaternary at 403.2 eV, along with NO_x species at 404.4 eV and 405.9 eV. The

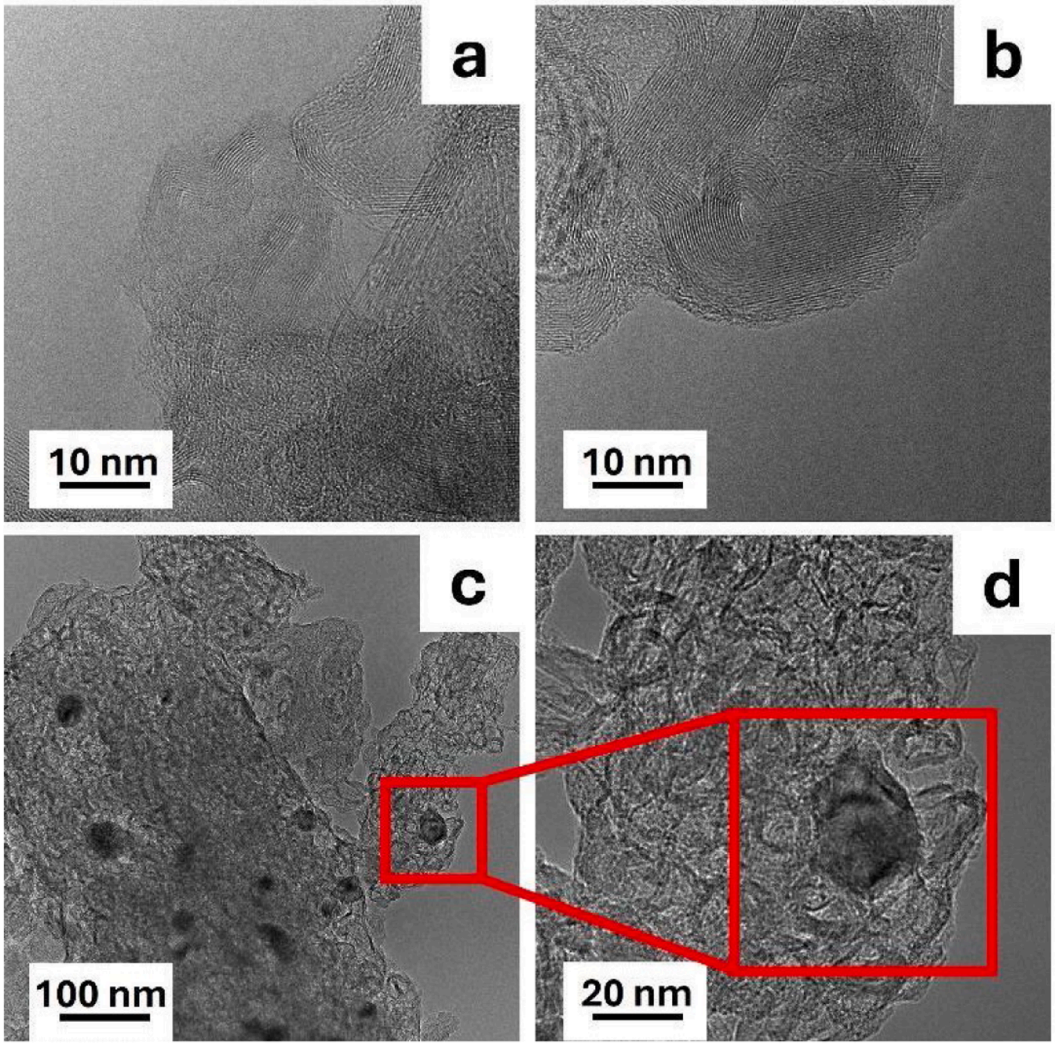

Fig. 2. TEM images of the FeNC electrocatalysts: a) FeNC$^{NaOH+HCl}$, b) FeNC^{HF}, c) FeNC^{Teflon} and d) FeNC^{Teflon}, focus on a Fe NPs.

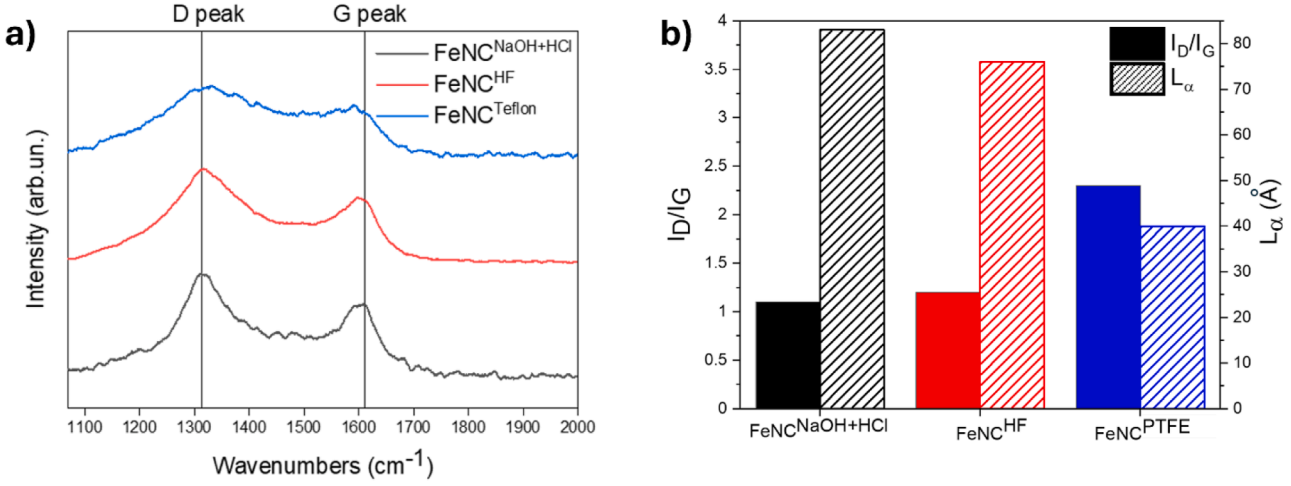

Fig. 3. a) Raman spectra in the range 1070–2000 cm^{-1} of FeNC$^{NaOH+HCl}$, FeNC^{HF}, and FeNC^{Teflon}. b) Comparison of I_D/I_G ratio and L_α trends.

relative atomic percentages of N 1 s are detailed in Table S1.

In Fig. 4, the detailed analysis of carbon 1 s spectra unveiled various carbon moieties: graphitic carbon at 284.5 eV, aliphatic carbon (C-C) at 285.2 eV, secondary carbon (C*-C-O) at 286.0 eV, C-O / C-N at 287.1 eV, C=O at 288.3 eV, COOH at 289.7 eV and two shoulders at 291.3 eV and 293 eV that can be ascribed to shake-up satellites of n-n* transitions of unsaturated species. The relative atomic percentages of C 1 s are outlined in Table S2. The XPS analysis confirmed the successful

Table 1
Surface atomic composition in at. % from XPS survey spectra.

At. %*	$FeNC^{NaOH+HCl}$	$FeNC^{HF}$	$FeNC^{Teflon}$
C 1s	84.5 ± 0.7	94.3 ± 0.1	94.1 ± 0.2
N 1s	1.2 ± 0.1	1.8 ± 0.2	1.1 ± 0.0
N/C	0.0142 ± 0.0001	0.0191 ± 0.0002	0.0117 ± 0.0000
O 1s	10.0 ± 0.4	3.7 ± 0.2	4.5 ± 0.2
Si 2p	4.3 ± 0.3	0.2 ± 0.1	0.3 ± 0.0

* The Fe content could not be taken into account in this ratio. The atomic composition should be taken as a relative indication among materials.

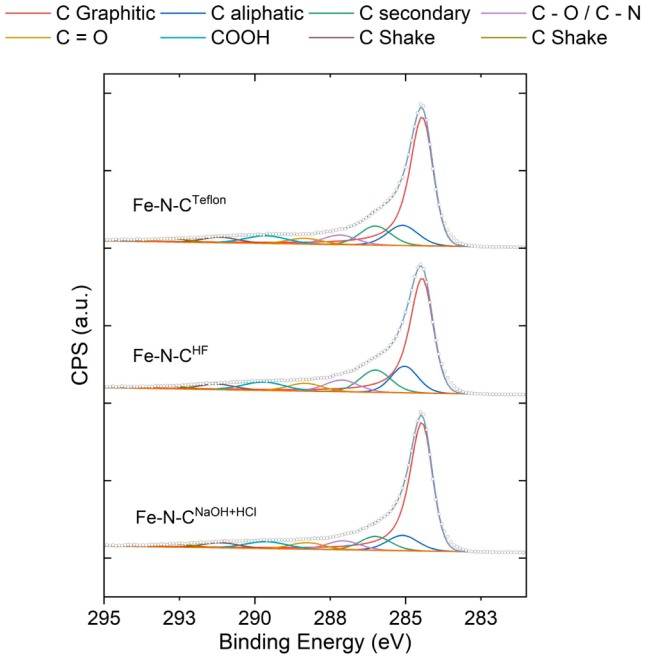

Fig. 4. Detailed C 1 s spectra of different FeNC catalysts.

incorporation of defects in the carbonaceous structure of the materials, with a high atomic percentage of C-O /C-N bonds from the C 1 s spectra (rel. at. % > 5.6) and Fe-N coordination from the N 1 s spectra (rel. at. % > 9.80), which is representative of the single atom sites.

In contrast to previous findings [26,40], the iron content was not detected. This can be explained by considering that i. the near-surface sensitivity of XPS for Fe corresponds to a sampling depth of about 1.5 nm, much lower than that of N of about 11 nm [41], and ii. the expected atomic percentage of Fe is much lower compared to the other elements for FeNC electrocatalysts and close to the XPS resolution. To overcome these issues, iron content was evaluated through ICP-MS analysis. The two materials without iron nanoparticles have a similar Fe content, with 0.41±0.05 wt. % and 0.31±0.05 wt. % for $FeNC^{NaOH+HCl}$ and $FeNC^{HF}$ respectively. For the Teflon-treated material, the Fe content is 6.03 ±0.05 wt. %, indicating that almost no Fe species have been leached.

The isotherms and the specific surface area were evaluated through N_2-sorption analysis. Fig. 5a presents the adsorption-desorption curves for both the FeNC samples and the silica template, classified as type IV isotherms. This behavior is characteristic of mesoporous channel structures, further confirming the successful impregnation of the precursor solution within the mesoporous silica template. However, the NaOH+HCl- and HF-treated electrocatalysts show an initial steep rise at very low relative pressures (p/p^0<0.1), suggesting the presence of considerable micropores. They cause a significant uptake of gas at low relative pressures due to the strong adsorption forces in very small pores. Then, a knee can be observed related to the monolayer adsorption capacity from which it is possible to evaluate the specific surface area. Going to higher p/p^0 values, pore condensation starts to occur. For increasing pressure, the density of the gas in the pores also increases until it condensates and turns to liquid at a pressure lower than the saturation pressure of the bulk liquid [42]. At higher relative pressure ($p/p^0 > 0.4$), the presence of a hysteresis and the capillary condensation phenomenon allow to classify the isotherms as a IVa type. Usually, type IV isotherms end with a final saturation plateau related to a complete mesopores filling. In our case, the plateau is not reached and this can be ascribed to incomplete pores filling because of interparticle spaces. The isotherm curves for the Teflon-treated sample show lower nitrogen adsorption compared to the other two samples, suggesting that it has fewer accessible pores and lower overall porosity. This is even confirmed by the adsorption cumulative pores volume achieved through BJH analysis, which are 1.04, 0.95, and 0.54 $cm^3\ g^{-1}$ for $FeNC^{NaOH+HCl}$, $FeNC^{HF}$, and $FeNC^{Teflon}$, respectively. To further justify this point, the pore size distribution curves (Fig. S4) show that all samples exhibit a dominant peak at around 3–4 nm, characteristic of SBA-15-derived mesoporous carbon structures [43]. However, $FeNC^{HF}$ displays a slightly higher incremental pore volume in this range, which aligns with its higher nitrogen adsorption compared to $FeNC^{Teflon}$. The lower incremental pore volume of $FeNC^{Teflon}$ within this critical range suggests a reduced availability of mesopores, further explaining the lower adsorption capacity. Finally, in Fig. 5b it is possible to appreciate the electrocatalyst specific surface areas evaluated with the BET model. We

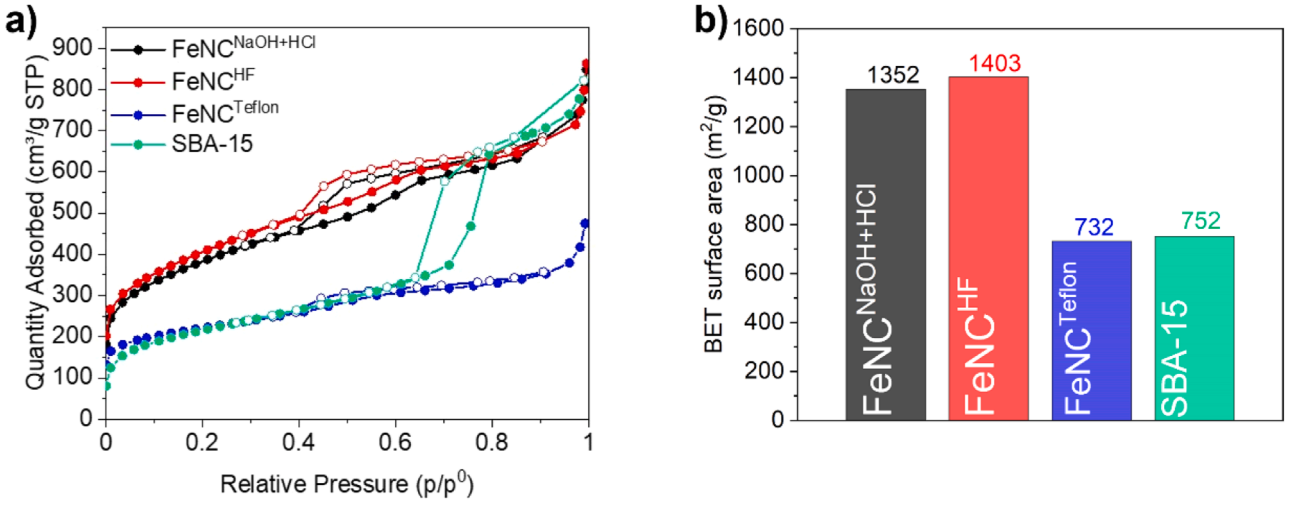

Fig. 5. a) N_2-adsorption (close circles) -desorption (open circles) isotherms and b) BET specific surface areas.

can observe high surface areas of ~1400 m^2 g^{-1} for both $FeNC^{NaOH+HCl}$ and $FeNC^{HF}$ samples, as it will also be observed later in the electrochemical characterization (Fig. S5). The BET specific surface areas for these two catalysts are higher than the one reported for the SBA-15 template (752 m^2 g^{-1}), suggesting the introduction of additional microporosity, as already indicated by the isotherms' steep rise at $p/p^0 < 0.1$. During the high-temperature pyrolysis step, the organic precursors decompose, leading to the formation of a carbon network and resulting in the release of volatile compounds. As these gases are released, they leave behind micropores within the carbon matrix, which increase the specific surface area. This situation does not apply to the Teflon-treated sample where a lower BET specific surface area of 732 m^2 g^{-1} is achieved. The decomposition of Teflon and the subsequent removal of the silica template occurred at temperatures lower than those required for graphitization, which is necessary to develop a well-defined and interconnected porous carbon structure. Since the removal of the template happens too early, it can cause local structural collapse or compaction. The resulting electrocatalyst structure may be less porous and less uniform, leading to a lower overall surface area [27].

3.2. RRDE performance

The electrocatalytic activities in terms of ORR of the FeNC samples were assessed in both acidic (0.1 M $HClO_4$) and alkaline (0.1 M KOH) media in a RDE setup, performing CV in both N_2- and O_2-saturated solutions and LSV at 1600 rpm in an oxygen atmosphere. At first, the ORR activity was investigated in terms of CV run at 100 mV s^{-1} as reported in Fig. S5, where the performances of the materials in N_2- and O_2-saturated solutions can be compared. For the curves achieved in a N_2-saturated atmosphere, information about the capacitive background can be achieved. Its extension can be attributed to the very high specific surface area measured during N_2-sorption analyses, linked to the double-layer interface and consequently assigned to the electrostatic double-layer capacitance. No redox peaks are visible for the samples without Fe nanoparticles, demonstrating the absence of electrochemical reactions in the inert atmosphere. However, for the $FeNC^{Teflon}$ sample, peaks in the positive and negative potential scans are visible, with a peak maximum in the 0.6–0.8 V_{RHE} range. This redox couple has been assessed to both the Fe^{2+}/Fe^{3+} redox or to carbon quinone/hydroquinone reaction [44]. In our case, we related the redox couple to the presence of iron nanoparticles, as shown by the TEM and XRD analyses. By looking at the data collected in O_2-saturated environments, a well-defined reduction peak appears, witnessing the reduction of the dissolved oxygen in the electrolytic solution. For the $HClO_4$ case, a reduction peak can be observed in the 0.6–0.8 V_{RHE} range, while a peak in the 0.7–0.9 V_{RHE} range is appreciated in the KOH media. These peaks are in trend with data achieved for the state-of-the-art FeNC materials [31,45–47]. LSV curves at 400, 900, 1600, and 2500 rpm for the $FeNC^{NaOH+HCl}$ electrocatalyst are shown in Fig. S6, while Fig. 6a and 6b provides the LSV of each sample at 1600 rpm for performance comparison. Both onset and halfwave potentials are reported in Table 2 to quantify the electrocatalytic performances. Here, the onset potential is defined as the potential at -0.1 mA/cm^2, while the halfwave potential is the potential at which the current reaches half of its limiting value. $FeNC^{NaOH+HCl}$ and $FeNC^{HF}$ show very similar performances in both media. This demonstrates that both leaching techniques are effective and lead to materials with comparable amounts of accessible active sites. However, among the two samples, $FeNC^{NaOH+HCl}$ results to be the

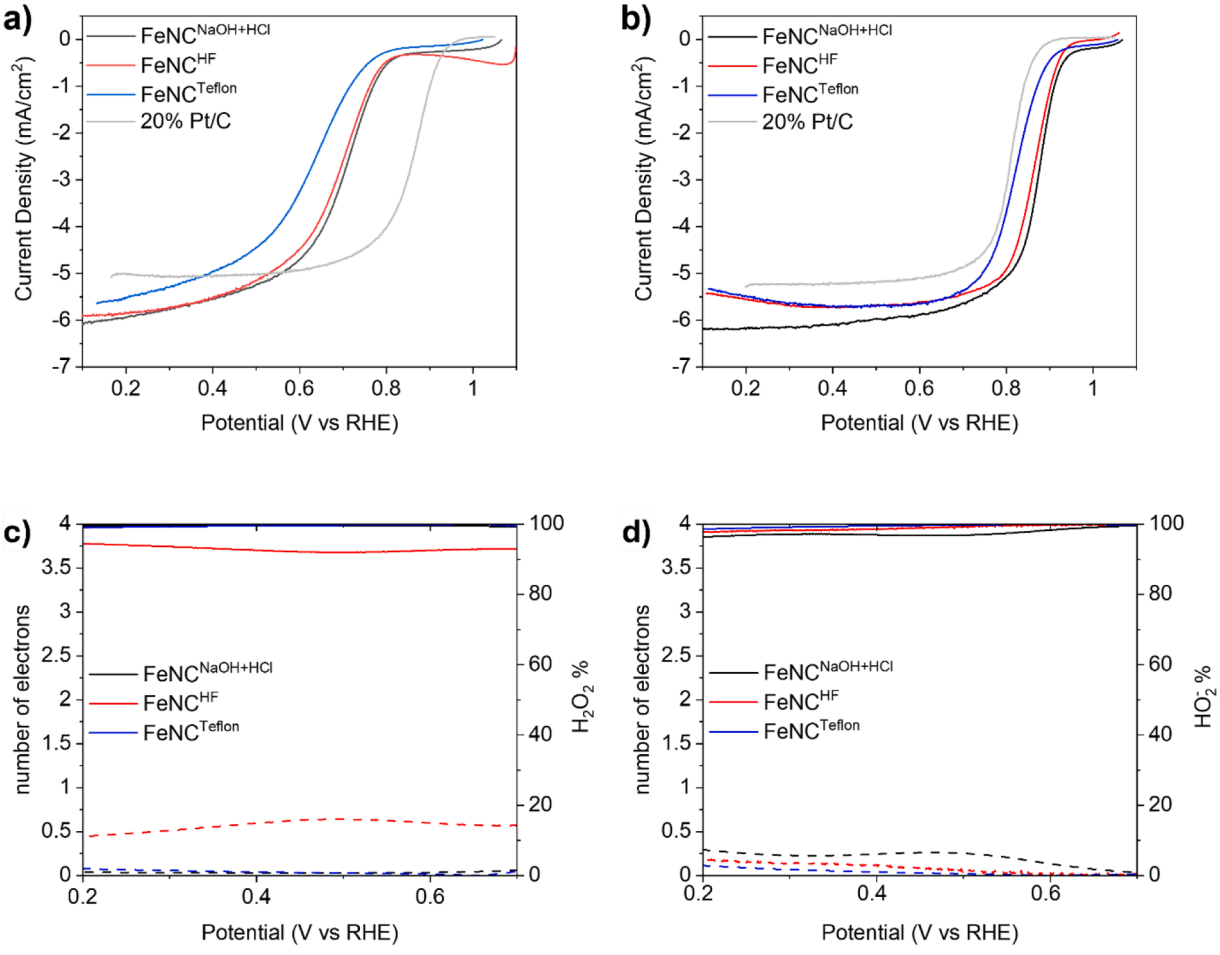

Fig. 6. a) ORR electrocatalytic activity of the samples in acid and b) alkaline environments. c) ORR selectivity by RRDE measurement in acid and d) alkaline media.

Table 2
Onset and halfwave potentials vs RHE for the proposed sample obtained from the LSV curves.

	$FeNC^{NaOH+HCl}$		$FeNC^{HF}$		$FeNC^{Teflon}$		20 % Pt/C	
electrolyte	$HClO_4$	KOH	$HClO_4$	KOH	$HClO_4$	KOH	$HClO_4$	KOH
Onset Potential [V_{RHE}]	0.81 ± 0.02	0.93 ± 0.01	0.80 ± 0.03	0.92 ± 0.02	0.76 ± 0.04	0.89 ± 0.03	0.92 ± 0.03	0.81 ± 0.02
Halfwave Potential [V_{RHE}]	0.71 ± 0.04	0.87 ± 0.02	0.65 ± 0.04	0.86 ± 0.03	0.64 ± 0.05	0.81 ± 0.03	0.83 ± 0.04	0.81 ± 0.04

most performant, with an onset potential of 0.93 V_{RHE} in the alkaline solution, and 0.81 V_{RHE} in the acidic case. In the alkaline environment, its performance is greater than that of the Pt/C commercial reference that was tested in the same set-up with conventional loadings for such materials (12 μg_{Pt} cm^{-2}). The superior performance in alkaline media compared to that in the acidic electrolyte is well reported in the literature [48,49]. The performance in acidic media of $FeNC^{NaOH+HCl}$ and $FeNC^{HF}$ matches with that of state-of-the-art FeNC catalysts (see Table 3). The Teflon-treated sample exhibits the lowest activity, which can be reasonably attributed to its 50 % reduction in surface area compared to the other two samples, as determined by BET analysis. Finally, Fig. S6 provides insights into how the rotation rate of the disk electrode significantly affects the mass transport of oxygen in the electrolyte to the catalyst surface. At high potentials, current density is unaffected by rotation, indicating that electron-transfer kinetics is the rate-determining step. As the potential decreases, rotation influences the current due to increased mass diffusion and oxygen availability. At very low potentials, oxygen diffusion becomes the limiting factor, leading to a plateau that reflects the diffusion-convection limiting current.

To investigate the ORR pathway of the samples, the selectivity of the electrocatalysts toward the four-electron reduction reaction was investigated with a rotating ring disk electrode (RRDE) setup. If hydrogen peroxide is formed at the surface of the disk, part of it can escape the surface and react at the surface of the ring (Pt) with a 2-electron pathway. Ring and disk currents are used to compute the number of electrons involved in the reduction reaction (eq. 6) and the consequent amount of peroxide species (eq. 7), responsible for the indirect two-electron pathway.

$$n = 4 \times \frac{I_D}{I_D + \frac{I_R}{N}} \tag{6}$$

$$HO_2^-\%\,(H_2O_2\%) = 200 \times \frac{\frac{I_R}{N}}{I_D + \frac{I_R}{N}} \tag{7}$$

I_D and I_R are respectively the disk and the ring currents measured with LSV at 1600 rpm, while N is the collection efficiency at the platinum ring equal to 0.37 for the employed RRDE setup. Fig. 6c and 6d shows the selectivity of the catalysts along the potential range, while Fig. S7 reports the ring currents employed in equations 6 and 7. All samples in both acidic and alkaline media demonstrate high selectivity toward the 4-electron reduction pathway, aligning with previous studies (see Table 3). The resulting minimal hydrogen peroxide formation is essential for the material's practical application as a fuel cell cathode. Indeed, looking at the performances in acidic media (Fig. 6c), which is also the typical environment of a fuel cell, we can observe that the amount of peroxide is below 5 %, in agreement with other literature results [56]. The only catalyst that exhibits different performances is the one treated with HF and tested in acidic conditions. Here, the ring current is higher than the other two (Fig. S7a), resulting in an increased percentage of peroxide species (around 15 %). These results specifically highlight the effectiveness of NaOH+HCl treatments in achieving high ORR activity and selectivity toward the four-electron pathway. To further validate the selectivity of the $FeNC^{NaOH+HCl}$ sample, the KL theory is applied to estimate the number of electrons transferred during the ORR, following the procedure outlined in the Supporting Information. From the slopes of the KL plots shown in Fig. S8, average electron transfer numbers of 3.8 and 3.7 are obtained in the 0.2–0.4 V_{RHE} potential range for the acidic and alkaline conditions, respectively. These values align with those derived from RRDE measurements (Fig. 6c and 6d), confirming the reliability of the KL model.

The stability of the most performant catalyst, $FeNC^{NaOH+HCl}$, was evaluated through CA measurements in both alkaline and acidic media. As shown in Fig. 7, the catalyst exhibits superior stability in alkaline conditions, retaining over 90 % of its initial current density after 4 hours. In contrast, a more pronounced degradation is observed in acidic media, with a current loss exceeding 20 %. This reduced acid stability can be attributed to the dissolution of Fe-based active sites, carbon corrosion, and the formation of aggressive peroxide intermediates, which accelerate catalyst degradation [57,58]. This highlights the intrinsic vulnerability of FeNC catalysts under acidic environments, reinforcing the challenge of their implementation in PEM fuel cells.

Table 3
Literature review of FeNC-based electrocatalysts for ORR applications.

Catalyst	Load (mg cm^{-2})	$E_{1/2}$ (V_{RHE})	Electron Transfer Number	Electrolyte	Ref.
M_{15}-FeNC-NH_3	0.8	0.782	3.9 @0.4 V_{RHE}	0.1 M $HClO_4$	[50]
FeNC	0.8	0.740 0.850	–	0.5 M H_2SO_4 0.1 M KOH	[51]
Fe-SA/PC-700-5	0.2	0.910	4 @0.2–0.8 V_{RHE}	0.1 M KOH	[52]
AT-BP-E	0.6	0.780	3.85 @0.4 V_{RHE}	0.1 M $HClO_4$	[53]
meso-Fe-N-C	0.4	0.846	3.9 @0.45 V_{RHE}	0.1 M KOH	[54]
Fe-NMP	0.6	0.840	–	0.1 M KOH	[40]
Fe/N/C	0.1	0.845	4 @0.6 V_{RHE}	0.1 M KOH	[55]
$FeNC^{NaOH+HCl}$	0.4	0.810 0.930	4 @0.4 V_{RHE} 3.95 @0.4 V_{RHE}	0.1 M $HClO_4$ 0.1 M KOH	This work

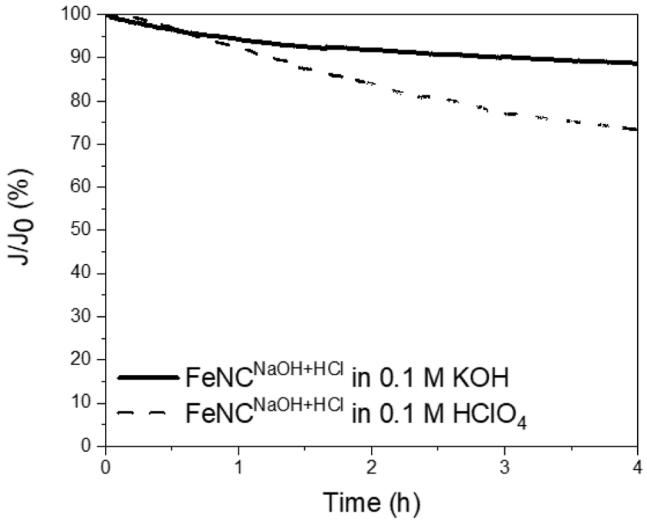

Fig. 7. i-t curves for $FeNC^{NaOH+HCl}$ achieved at 0.68 $_{VRHE}$ in both acidic and alkaline media.

4. Conclusions

This study demonstrated that different synthesis approaches significantly impact the performance of FeNC electrocatalysts for the oxygen reduction reaction in low-temperature fuel cell. Among the three strategies explored—acid leaching with hydrofluoric acid, basic leaching with sodium hydroxide followed by hydrochloric acid treatment, and an acid-free Teflon-assisted method—the NaOH+HCl approach provided the most promising results. This method not only ensured efficient removal of silica templates and metallic impurities but also maintained a high surface area and porosity, essential for enhancing catalytic activity.

The HF-based method, while effective in removing silica and increasing surface area and porosity, raises significant environmental and safety concerns due to HF's toxicity. In contrast, the Teflon-assisted method, although acid-free and potentially more sustainable, was less effective in enhancing surface area and porosity, which adversely affected the electrocatalyst's overall performance.

Electrochemical characterization showed that the $FeNC^{NaOH+HCl}$ electrocatalyst exhibited superior ORR activity in both acidic and alkaline environments, surpassing the performance of a commercial platinum-based electrocatalyst in alkaline conditions. This electrocatalyst's performance aligns well with state-of-the-art FeNC electrocatalysts, confirming its potential for practical applications in PEMFCs.

Overall, these results highlight the importance of optimizing the synthesis method of FeNC electrocatalysts to balance performance, sustainability, and safety. The NaOH+HCl approach appears to offer a viable pathway for developing cost-effective and efficient FeNC electrocatalysts, advancing the commercialization of PEM fuel cells while minimizing environmental impact.

CRediT authorship contribution statement

Giulia Gianola: Writing – original draft, Methodology, Investigation, Formal analysis, Data curation. **Alessio Cosenza:** Writing – original draft, Methodology, Investigation, Formal analysis. **Camille Roiron:** Writing – review & editing, Methodology, Investigation, Conceptualization. **Candido F. Pirri:** Supervision, Funding acquisition. **Stefania Specchia:** Writing – review & editing, Supervision, Resources, Formal analysis. **Plamen Atanassov:** Writing – review & editing, Supervision, Resources, Funding acquisition, Formal analysis. **Juqin Zeng:** Writing – review & editing, Supervision, Methodology, Formal analysis.

Declaration of competing interest

The authors declare that they have no known competing financial interests or personal relationships that could have appeared to influence the work reported in this paper.

Acknowledgements

G.G. acknowledges the international mobility program Erasmus+/Partner Countries academic year 2023/2024, grant n. 2022-1-IT02-KA171-HED-000074319, for supporting her stay at UCI in 2023/2024. J.Z. received the fund under the National Recovery and Resilience Plan (NRRP) - Project code: IR0000027, Concession Decree No. 128 of 21/06/2022 adopted by the Italian Ministry of Research, CUP: B33C22000710006, Project title: iENTRANCE.

Supplementary materials

Supplementary material associated with this article can be found, in the online version, at doi:10.1016/j.electacta.2025.146085.

Data availability

Data will be made available on request.

References

[1] M.K. Debe, Electrocatalyst approaches and challenges for automotive fuel cells, Nature 486 (2012) 43–51, https://doi.org/10.1038/nature11115.
[2] Z. Chen, D. Higgins, A. Yu, L. Zhang, J. Zhang, A review on non-precious metal electrocatalysts for PEM fuel cells, Energy Environ. Sci. 4 (2011) 3167–3192, https://doi.org/10.1039/c0ee00558d.
[3] I. Bar-On, R. Kirchain, R. Roth, Technical cost analysis for PEM fuel cells, J. Power Sources 109 (2002) 71–75.
[4] Y. Wang, D.F. Ruiz Diaz, K.S. Chen, Z. Wang, X.C. Adroher, Materials, technological status, and fundamentals of PEM fuel cells – A review, Mater. Today 32 (2020) 178–203, https://doi.org/10.1016/j.mattod.2019.06.005.
[5] Y. Nie, L. Li, Z. Wei, Recent advancements in Pt and Pt-free catalysts for oxygen reduction reaction, Chem. Soc. Rev. 44 (2015) 2168–2201, https://doi.org/10.1039/c4cs00484a.
[6] S. Stariha, K. Artyushkova, M.J. Workman, A. Serov, S. Mckinney, B. Halevi, P. Atanassov, PGM-free Fe-N-C catalysts for oxygen reduction reaction: catalyst layer design, J. Power Sources 326 (2016) 43–49, https://doi.org/10.1016/j.jpowsour.2016.06.098.
[7] R. Venegas, K. Muñoz-Becerra, C. Candia-Onfray, J.F. Marco, J.H. Zagal, F.J. Recio, Experimental reactivity descriptors of M-N-C catalysts for the oxygen reduction reaction, Electrochim. Acta 332 (2020), https://doi.org/10.1016/j.electacta.2019.135340.
[8] A.A. Gewirth, J.A. Varnell, A.M. Diascro, Nonprecious metal catalysts for oxygen reduction in heterogeneous aqueous systems, Chem. Rev. 118 (2018) 2313–2339, https://doi.org/10.1021/acs.chemrev.7b00335.
[9] Y. Sun, S. Polani, F. Luo, S. Ott, P. Strasser, F. Dionigi, Advancements in cathode catalyst and cathode layer design for proton exchange membrane fuel cells, Nat. Commun. 12 (2021) 1–14, https://doi.org/10.1038/s41467-021-25911-x.
[10] X. Cui, W. Li, P. Ryabchuk, K. Junge, M. Beller, Bridging homogeneous and heterogeneous catalysis by heterogeneous single-metal-site catalysts, Nat. Catal. 1 (2018) 385–397, https://doi.org/10.1038/s41929-018-0090-9.
[11] T. Asset, P. Atanassov, Iron-nitrogen-carbon catalysts for proton exchange membrane fuel cells, Joule 4 (2020) 33–44, https://doi.org/10.1016/j.joule.2019.12.002.
[12] J. Liu, Z. Jin, X. Wang, J. Ge, C. Liu, W. Xing, Recent advances in active sites identification and regulation of M-N/C electro-catalysts towards ORR, Sci. China Chem. 62 (2019) 669–683, https://doi.org/10.1007/s11426-018-9425-5.
[13] J.H. Zagal, S. Specchia, P. Atanassov, Mapping transition metal-MN4 macrocyclic complex catalysts performance for the critical reactivity descriptors, Curr. Opin. Electrochem. 27 (2021), https://doi.org/10.1016/j.coelec.2020.100683.
[14] S. Specchia, P. Atanassov, J.H. Zagal, Mapping transition metal–nitrogen–carbon catalyst performance on the critical descriptor diagram, Curr. Opin. Electrochem. 27 (2021), https://doi.org/10.1016/j.coelec.2021.100687.
[15] Y. Xiong, H. Li, C. Liu, L. Zheng, C. Liu, J.O. Wang, S. Liu, Y. Han, L. Gu, J. Qian, D. Wang, Single-atom Fe catalysts for fenton-like reactions: roles of different N species, Adv. Mater. 34 (2022), https://doi.org/10.1002/adma.202110653.
[16] H.S. Hu, R.J. Liu, S. Si, D.S. Kong, Y.Y. Feng, Iron and nitrogen codoped carbon catalyst with excellent stability and methanol tolerance for oxygen reduction reaction, Int. J. Energy Res. 43 (2019) 7107–7119, https://doi.org/10.1002/er.4734.
[17] P.G. Santori, F.D. Speck, J. Li, A. Zitolo, Q. Jia, S. Mukerjee, S. Cherevko, F. Jaouen, Effect of pyrolysis atmosphere and electrolyte pH on the oxygen reduction activity, stability and spectroscopic signature of FeN x moieties in Fe-N-C catalysts, J. Electrochem. Soc. 166 (2019) F3311–F3320, https://doi.org/10.1149/2.0371907jes.
[18] A. Serov, K. Artyushkova, P. Atanassov, Fe-N-C oxygen reduction fuel cell catalyst derived from carbendazim: synthesis, structure, and reactivity, Adv. Energy Mater. 4 (2014), https://doi.org/10.1002/aenm.201301735.
[19] A.H.A. Monteverde Videla, L. Osmieri, M. Armandi, S. Specchia, Varying the morphology of Fe-N-C electrocatalysts by templating iron phthalocyanine precursor with different porous SiO2 to promote the Oxygen Reduction Reaction, Electrochim. Acta 177 (2015) 43–50, https://doi.org/10.1016/j.electacta.2015.01.165.
[20] L. Osmieri, A.H.A. Monteverde Videla, M. Armandi, S. Specchia, Influence of different transition metals on the properties of me–N–C (Me = Fe, Co, Cu, Zn) catalysts synthesized using SBA-15 as tubular nano-silica reactor for oxygen reduction reaction, Int. J. Hydrogen Energy 41 (2016) 22570–22588, https://doi.org/10.1016/j.ijhydene.2016.05.223.
[21] C. Roiron, C. Celle, P.A. Jacques, M. Heitzmann, J.P. Simonato, Structure-property relationship of cryogel-based Fe-N-C catalysts for the oxygen reduction reaction, Energy and Fuels 35 (2021) 16814–16821, https://doi.org/10.1021/acs.energyfuels.1c02580.
[22] Y. He, Q. Tan, L. Lu, J. Sokolowski, G. Wu, Metal-nitrogen-carbon catalysts for oxygen reduction in PEM fuel cells: self-template synthesis approach to enhancing catalytic activity and stability, Electrochem. Energy Rev. 2 (2019) 231–251, https://doi.org/10.1007/s41918-019-00031-9.
[23] P.S. Shinde, P.S. Suryawanshi, K.K. Patil, V.M. Belekar, S.A. Sankpal, S.D. Delekar, S.A. Jadhav, A brief overview of recent progress in porous silica as catalyst supports, J. Compos. Sci. 5 (2021) 1–17, https://doi.org/10.3390/jcs5030075.
[24] J.K. Kang, C.B. Musgrave, The mechanism of HF/H2O chemical etching of SiO2, J. Chem. Phys. 116 (2002) 275–280, https://doi.org/10.1063/1.1420729.
[25] D. Wu, Z. Li, M. Zhong, T. Kowalewski, K. Matyjaszewski, Templated synthesis of nitrogen-enriched nanoporous carbon materials from porogenic organic precursors prepared by ATRP, Angew. Chemie - Int. Ed. 53 (2014) 3957–3960, https://doi.org/10.1002/anie.201309836.

[26] A. Cosenza, L. Delafontaine, A. Ly, H. Wang, E. Murphy, Y. Liu, S. Specchia, P. Atanassov, Novel acid-free process intensification for the synthesis of non-precious metal-nitrogen-carbon electrocatalysts for oxygen reduction reaction, J. Power Sources 556 (2023), https://doi.org/10.1016/j.jpowsour.2022.232382.
[27] Y. Liang, Q. Cao, M. Zheng, H. Huo, H. Hu, H. Dong, Y. Xiao, Y. Liu, Teflon: A decisive additive in directly fabricating hierarchical porous carbon with network structure from natural leaf, ACS Sustain. Chem. Eng. 5 (2017) 9307–9312, https://doi.org/10.1021/acssuschemeng.7b02318.
[28] D.K. Singh, K.S. Krishna, S. Harish, S. Sampath, M. Eswaramoorthy, No more HF: teflon-assisted ultrafast removal of silica to generate high-surface-area mesostructured carbon for enhanced CO 2 capture and supercapacitor performance, Angew. Chemie 128 (2016) 2072–2076, https://doi.org/10.1002/ange.201509054.
[29] M. Ferrandon, A.J. Kropf, D.J. Myers, K. Artyushkova, U. Kramm, P. Bogdanoff, G. Wu, C.M. Johnston, P. Zelenay, Multitechnique characterization of a polyaniline-iron-carbon oxygen reduction catalyst, J. Phys. Chem. C 116 (2012) 16001–16013, https://doi.org/10.1021/jp302396g.
[30] U.I. Kramm, I. Herrmann-Geppert, P. Bogdanoff, S. Fiechter, Effect of an ammonia treatment on structure, composition, and oxygen reduction reaction activity of Fe-N-C catalysts, J. Phys. Chem. C 115 (2011) 23417–23427, https://doi.org/10.1021/jp207417y.
[31] H. Shen, T. Thomas, S.A. Rasaki, A. Saad, C. Hu, J. Wang, M. Yang, Oxygen reduction reactions of Fe-N-C catalysts: current status and the way forward, Electrochem. Energy Rev. 2 (2019) 252–276, https://doi.org/10.1007/s41918-019-00030-w.
[32] U.I. Kramm, A. Zana, T. Vosch, S. Fiechter, M. Arenz, D. Schmeißer, On the structural composition and stability of Fe–N–C catalysts prepared by an intermediate acid leaching, J. Solid State Electrochem. 20 (2016) 969–981, https://doi.org/10.1007/s10008-015-3060-z.
[33] H. Zhao, H. Han, Synthesis and characterization of functionalized SBA-15 silica through template removal, J. Solid State Chem. 282 (2020) 121074, https://doi.org/10.1016/j.jssc.2019.121074.
[34] G. Jaiswal, V.G. Landge, D. Jagadeesan, E. Balaraman, Sustainable iron-catalyzed direct imine formation by acceptorless dehydrogenative coupling of alcohols with amines, Green Chem. 18 (2016) 3232–3238. https://doi.org/10.1039/c6gc00565a.
[35] F. TUINSTRA, J.L. KOENIG, Raman Spectrum of Graphite, J. Chem. Phys. 53 (1970) 1126–1130, https://doi.org/10.1063/1.1674108.
[36] L. Delafontaine, A. Cosenza, E. Murphy, Y. Liu, J. Chen, B. Sun, P. Atanassov, Metal-nitrogen-carbon catalysts by dynamic template removal for highly efficient and selective electroreduction of CO2, ACS Appl. Energy Mater. 6 (2023) 678–691, https://doi.org/10.1021/acsaem.2c02811.
[37] R. Gokhale, Y. Chen, A. Serov, K. Artyushkova, P. Atanassov, Direct synthesis of platinum group metal-free Fe-N-C catalyst for oxygen reduction reaction in alkaline media, Electrochem. Commun. 72 (2016) 140–143, https://doi.org/10.1016/j.elecom.2016.09.013.
[38] S. Kabir, K. Artyushkova, A. Serov, B. Kiefer, P. Atanassov, Binding energy shifts for nitrogen-containing graphene-based electrocatalysts - experiments and DFT calculations, Surf. Interface Anal. 48 (2016) 293–300, https://doi.org/10.1002/sia.5935.
[39] M. Huang, R. Ding, J. Yang, W. Shi, S. Shi, L. Chen, S. Liu, X. Yin, Formation of nitrogen-coordinated metal sites (M = Fe, Co) via solution-phase coordination on nickel- and nitrogen-Co-doped carbon templates with metal vacancy-N x sites, J. Electrochem. Soc. 169 (2022) 106507, https://doi.org/10.1149/1945-7111/ac96a9.
[40] M.M. Hossen, K. Artyushkova, P. Atanassov, A. Serov, Synthesis and characterization of high performing Fe-N-C catalyst for oxygen reduction reaction (ORR) in Alkaline Exchange membrane fuel cells, J. Power Sources 375 (2018) 214–221, https://doi.org/10.1016/j.jpowsour.2017.08.036.
[41] A. Serov, M.J. Workman, K. Artyushkova, P. Atanassov, G. McCool, S. McKinney, H. Romero, B. Halevi, T. Stephenson, Highly stable precious metal-free cathode catalyst for fuel cell application, J. Power Sources 327 (2016) 557–564, https://doi.org/10.1016/j.jpowsour.2016.07.087.
[42] M. Thommes, K. Kaneko, A.V. Neimark, J.P. Olivier, F. Rodriguez-Reinoso, J. Rouquerol, K.S.W. Sing, Physisorption of gases, with special reference to the evaluation of surface area and pore size distribution (IUPAC Technical Report), Pure Appl. Chem. 87 (2015) 1051–1069, https://doi.org/10.1515/pac-2014-1117.
[43] J. Zeng, C. Francia, M.A. Dumitrescu, A.H.A. Monteverde Videla, V.S. Ijeri, S. Specchia, P. Spinelli, Electrochemical performance of Pt-based catalysts supported on different ordered mesoporous carbons (Pt/OMCs) for oxygen reduction reaction, Ind. Eng. Chem. Res. 51 (2012) 7500–7509, https://doi.org/10.1021/ie2016619.
[44] T. Marshall-Roth, N.J. Libretto, A.T. Wrobel, K.J. Anderton, M.L. Pegis, N.D. Ricke, T. Van Voorhis, J.T. Miller, Y. Surendranath, A pyridinic Fe-N4 macrocycle models the active sites in Fe/N-doped carbon electrocatalysts, Nat. Commun. 11 (2020), https://doi.org/10.1038/s41467-020-18969-6.
[45] X. Yan, Y. Yao, Y. Chen, Highly active and stable Fe-N-C oxygen reduction electrocatalysts derived from electrospinning and In situ pyrolysis, Nanoscale Res. Lett. 13 (2018) 0–6, https://doi.org/10.1186/s11671-018-2635-x.
[46] S. Jerez, A. Pedersen, M. Ventura, L. Mazzoli, M.I. Pariente, M. Titirici, J.A. Melero, J. Barrio, Fe [sbnd]N doped carbon materials from oily sludge as electrocatalysts for alkaline oxygen reduction reaction, Electrochim. Acta 483 (2024) 144045, https://doi.org/10.1016/j.electacta.2024.144045.
[47] C. Chen, Y. Wu, X. Li, Y. Ye, Z. Li, Y. Zhou, J. Chen, M. Yang, F. Xie, Y. Jin, C. Jones, N. Wang, H. Meng, S. Chen, Modulating Fe spin state in FeNC catalysts by adjacent Fe atomic clusters to facilitate oxygen reduction reaction in proton exchange membrane fuel cell, Appl. Catal. B Environ. 342 (2024) 123407, https://doi.org/10.1016/j.apcatb.2023.123407.
[48] S. Brocato, A. Serov, P. Atanassov, PH dependence of catalytic activity for ORR of the non-PGM catalyst derived from heat-treated Fe-phenanthroline, Electrochim. Acta 87 (2013) 361–365, https://doi.org/10.1016/j.electacta.2012.09.053.
[49] S. Rojas-Carbonell, K. Artyushkova, A. Serov, C. Santoro, I. Matanovic, P. Atanassov, Effect of pH on the activity of platinum group metal-free catalysts in oxygen reduction reaction, ACS Catal. 8 (2018) 3041–3053, https://doi.org/10.1021/acscatal.7b03991.
[50] X. Xu, X. Zhang, Z. Xia, R. Sun, H. Li, J. Wang, S. Yu, S. Wang, G. Sun, Solid phase microwave-assisted fabrication of Fe-doped ZIF-8 for single-atom Fe-N-C electrocatalysts on oxygen reduction, J. Energy Chem. 54 (2021) 579–586, https://doi.org/10.1016/j.jechem.2020.06.046.
[51] K. Mamtani, C. Bruening, A.C. Co, U.S. Ozkan, A comparison of oxygen reduction reaction (ORR) performance for iron- nitrogen-carbon (FeNC) catalysts in acidic and alkaline Media, Res. Rev. Electrochem. 8 (2017) 1–9.
[52] J. Huo, L. Lu, Z. Shen, Y. Liu, J. Guo, Q. Liu, Y. Wang, H. Liu, M. Wu, G. Wang, A rational synthesis of single-atom iron-nitrogen electrocatalysts for highly efficient oxygen reduction reaction, J. Mater. Chem. A 8 (2020) 16271–16282, https://doi.org/10.1039/d0ta04798h.
[53] R. Ding, Y. Liu, Z. Rui, J. Li, J. Liu, Z. Zou, Facile grafting strategy synthesis of single-atom electrocatalyst with enhanced ORR performance, Nano Res. 13 (2020) 1519–1526, https://doi.org/10.1007/s12274-020-2768-y.
[54] Y. Zhou, Y. Yu, D. Ma, A.C. Foucher, L. Xiong, J. Zhang, E.A. Stach, Q. Yue, Y. Kang, Atomic Fe dispersed hierarchical mesoporous Fe-N-C nanostructures for an efficient oxygen reduction reaction, ACS Catal. 11 (2021) 74–81, https://doi.org/10.1021/acscatal.0c03496.
[55] Y. Wu, S. Nagata, Y. Nabae, Genuine four-electron oxygen reduction over precious-metal-free catalyst in alkaline media, Electrochim. Acta 319 (2019) 382–389, https://doi.org/10.1016/j.electacta.2019.06.174.
[56] F. Jaouen, J.P. Dodelet, O2 reduction mechanism on non-noble metal catalysts for PEM fuel cells. Part I: experimental rates of O2 electroreduction, H 2O2 electroreduction, and H2O2 disproportionation, J. Phys. Chem. C 113 (2009) 15422–15432, https://doi.org/10.1021/jp900837e.
[57] N. Yang, L. Peng, L. Li, J. Li, Q. Liao, M. Shao, Z. Wei, Theoretically probing the possible degradation mechanisms of an FeNC catalyst during the oxygen reduction reaction, Chem. Sci. 12 (2021) 12476–12484, https://doi.org/10.1039/d1sc02901k.
[58] C.H. Choi, H.K. Lim, M.W. Chung, G. Chon, N. Ranjbar Sahraie, A. Altin, M. T. Sougrati, L. Stievano, H.S. Oh, E.S. Park, F. Luo, P. Strasser, G. Dražić, K.J. J. Mayrhofer, H. Kim, F. Jaouen, The Achilles' heel of iron-based catalysts during oxygen reduction in an acidic medium, Energy Environ. Sci. 11 (2018) 3176–3182, https://doi.org/10.1039/c8ee01855c.